Available online at www.sciencedirect.com
SCIENCE DIRECT
Journal of Catalysis 234 (2005) 268–281
JOURNAL OF CATALYSIS
www.elsevier.com/locate/jcat

Catalytic hydrodechlorination over Pd supported on amorphous and structured carbon

Claudia Amorim [a], Guang Yuan [a], Patricia M. Patterson [b], Mark A. Keane [a,*]

[a] *Department of Chemical and Materials Engineering, University of Kentucky, Lexington, KY 40506, USA*
[b] *Center for Applied Energy Research, University of Kentucky, Lexington, KY 40506, USA*

Received 3 March 2005; accepted 5 June 2005

Available online 9 August 2005

Abstract

The gas phase catalytic hydrodechlorination (HDC) of chlorobenzene has been studied ($T = 423$ K) over Pd (8 ± 1wt%) supported on activated carbon (Pd/AC), graphite (Pd/graphite), and graphitic carbon nanofiber (Pd/GNF). The activated carbon (875 $m^2\ g^{-1}$) and graphite (11 $m^2\ g^{-1}$) substrates were obtained from a commercial source, but the carbon nanofibers (74 $m^2\ g^{-1}$) were synthesized by ethylene decomposition over unsupported Ni to yield a mean fiber diameter of 225 nm. Under identical reaction conditions, the following initial HDC activity sequence was established: Pd/GNF $\approx$ Pd/AC $>$ Pd/graphite. HDC activity declined with time-on-stream (four reaction cycles were considered), where Pd/GNF maintained a significantly higher fractional HDC and Pd/AC activity decreased continually to converge with Pd/graphite at a common residual conversion. The prereaction and postreaction catalyst samples were characterized by BET area/pore size analysis, temperature-programmed reduction, transmission electron microscopy, scanning electron microscopy, H_2 chemisorption/temperature-programmed desorption (TPD), X-ray diffraction (XRD), and acid/base titration. Pd size distribution is given in each case where surface area-weighted Pd diameter increased in the order: Pd/graphite $<$ Pd/GNF $<$ Pd/AC. The spent catalysts exhibited lower H_2 uptake with a disruption to the TPD profiles. Pd on each support adopted (on the basis of XRD analysis) an exclusive cubic geometry, but whereas the particles on AC were globular in nature, faceted Pd particles predominated on the graphite and (to a lesser extent) GNF supports. HDC activity and temporal behavior is rationalized on the basis of metal–support interactions, Pd particle size, and H_2 uptake/release characteristics.

Keywords: Hydrodechlorination; Chlorobenzene; Supported Pd; Activated carbon; Graphite; Carbon nanofibers

1. Introduction

The release of halogenated organics into the environment is associated with stratospheric ozone depletion, smog formation, global warming, and a range of human health effects [1]. Although such releases have been curtailed through stringent environmental regulations, chlorinated compounds still find widespread use (in, e.g., the manufacture of pesticides and degreasing agents) [2]. In previous reports [3–5], we demonstrated the viability of catalytic hydrodechlorination (HDC) over supported Ni as a nondestructive, low-energy method of converting toxic haloarene gas streams into recyclable raw materials. Chlorinated waste treatments based on electrochemical, radiation, photochemical, and biotechnological processes [6,7] result in low conversions and impractical scale-up. Thermal methods, including pyrolysis (>1200 K) and hydrogenolysis (>800 K), have high energy requirements [8,9]. Incineration can generate harmful dioxins/furans [1,6,7]. Catalytic HDC has now been reported in both liquid and gas phases over an array of catalysts, notably supported Pt [10–12], Ni [3–16], Rh [11,12], Ru [12,17], Ni–Mo [18], and Fe [19,20]. Group VIII noble metals are known to be effective in hydrogenolysis, and Pd has been demonstrated to deliver higher specific HDC rates [11,21]. Accordingly, we have adopted Pd as a model cat-

* Corresponding author. Present address: Chemical Engineering, School of Engineering and Physical Sciences, Heriot-Watt University, Edinburgh EH14 4AS, UK.
E-mail address: m.a.keane@hw.ac.uk (M.A. Keane).

0021-9517/$ – see front matter
doi:10.1016/j.jcat.2005.06.019

alytic agent in this fundamental study of the role of different forms of carbon support in determining Pd HDC performance.

Hydrogen-assisted dechlorination of aliphatic compounds has received much attention in the literature, with a particular focus on the conversion of chlorofluorocarbons [22,23] and chloroalkanes/chloroalkenes [10,24,25]. A distinction must be made between HDC and dehydrochlorination; the latter involves the internal elimination of HCl and is applicable to the dechlorination of aliphatic chloro compounds [26], where an external H_2 source is not necessary but can serve to limit deactivation [27]. HDC of chloroarenes has been considered to a lesser extent, but there are data available on the conversion of chlorobenzenes (CBs) [10,28], chlorophenols [29,30], and polychlorinated aromatics [31,32]. Catalyst deactivation is a feature of HDC in both liquid [33–36] and gas phase [21,37–44] operations, as a result of HCl interactions that poison the active metal [11,21,33,35,36,38,40,41]. The catalyst parameters that influence HDC performance include synthesis route [33,34], support [10,11,21,33,35], metal dispersion [11,33,34,38], metal loading [44], activation procedure [19,28,34,42,43], incorporation of additives [12,35,36,45], solvent [12,14,46], and the presence of a second metal (bimetallic catalysts) [19,21,28,39,41–43]. There is some evidence that the support can inhibit HCl poisoning [11,33]; in any case, the support must be resistant to the corrosive effects of high HCl concentrations generated at elevated temperatures [21]. Carbon [10,28] and inorganic supports, such as Al_2O_3 [10,37,42], SiO_2 [19,41], MgO [43], Nb_2O_5 [34], and AlF_3 [10], have been used in gas phase HDC of CB. The existing literature on chloroarene HDC over carbon-supported Pd is summarized in Table 1, where feasible, we relate our results to the trends that have emerged from the tabulated studies. We first note some reports that considered a series of supported Pd catalysts in CB HDC applications. Prati et al. [10] reported a clear dependence of activity on the nature of the support, yielding the following gas phase activity sequence: Pd/C > Pd/Vycor (porous glass) > Pd/Al_2O_3 > Pd/AlF_3. In the liquid phase, Benitez et al. [11] compared the HDC performance of supported Pd at a similar dispersion (7–10%), where Pd/SiO_2 > Pd/Al_2O_3 > Pd/C. In contrast, Halligudi et al. [44] reported the following order of decreasing 1,2-dichlorobenzene HDC: Pd/Al_2O_3 > Pd/C > Pd/SiO_2 > Pd/MgO. These results point to a support effect, but the source/cause has not yet been established.

The present study was conducted to couple characterization and catalytic data to probe the role of carbon structural characteristics in determining Pd HDC performance. Three carbonaceous supports were considered: conventional activated carbon, graphite, and GNFs. Carbon nanofibers, produced by the catalytic decomposition of carbon-containing gases at high temperatures, exhibit a high-aspect ratio with ordered parallel graphene layers arranged in a specific conformation [56,57]. Interest in GNF as a catalyst support has risen over the last decade, due largely to reduced mass transfer constraints when compared with conventional activated carbon, which exhibits variable structural characteristics when produced from disparate sources [56,58–61]. The use of GNF supports in hydrogenation reactions [56,57,60,62,63] and ammonium synthesis [64] has been recorded in the literature, but there has been no published study of catalytic HDC. In addition, there are no reports of Pd/graphite use in HDC. Here we provide the first account of Pd/graphite- and Pd/GNF-promoted CB HDC.

2. Experimental

2.1. Catalyst preparation and activation

The activated carbon (G-60, 100 mesh) was obtained from NORIT (UK), and the graphite (synthetic 1- to 2-μm powder) was obtained from Sigma–Aldrich. The GNF support was synthesized by the catalytic decomposition of ethylene over unsupported Ni, as described in detail previously [57]. The catalytically generated GNF product was contacted (agitation at 500 rpm) with dilute mineral acid (1 mol dm^{-3} HNO_3) for 7 days, to remove the parent catalyst particles. This step was necessary to avoid any contribution to HDC from residual Ni; the commercial activated carbon and graphite samples were also subjected to the same demineralization. The carbon supports were thoroughly washed with deionized water (until pH approached 7) and oven-dried at 383 K for 12 h. The GNF sample was subjected to partial oxidation (in a 5% v/v O_2/He mixture) at 673 K for 2 h to remove the amorphous carbon content. The carbon-supported (8 ± 1 wt%, ca. 1 at% Pd) Pd precursor samples were prepared by standard impregnation, in which a 2-butanolic $Pd(NO_3)_2$ solution was added dropwise at 353 K to the substrate with constant agitation (500 rpm), then air-dried at 393 K for 16 h. Aqueous solutions were not used, because carbon support materials are known to have hydrophobic properties leading to difficulties with surface wetting that may adversely affect the ultimate Pd dispersion. Moreover, the acid washing/partial oxidation can modify the wetting characteristics to provide anchoring sites for the supported metal [56,65]. The Pd loading (reproducible to within ±4%) was determined by ICP-OES (Vista-PRO, Varian). Before its use in catalysis, the precursor, sieved (ATM fine test sieves) into a batch of 75 μm average particle diameter, was reduced directly in a 60 cm^3 min^{-1} stream of ultrapure dry H_2 at 10 K min^{-1} to 523 ± 1 K, which was maintained for at least 12 h.

2.2. Catalyst characterization

Specific BET surface area and BJH pore volume analyses were performed using the commercial Micromeritics TriStar 3000 unit; N_2 at 77 K served as sorbate. Before measurement, the samples were outgassed at 433 K for 16 h. Bulk tap densities of the carbonaceous supports were obtained from a gravimetric measurement of

Table 1
Compilation of existing literature on chloroarene HDC over carbon supported Pd catalysts

Reactant	Catalyst	Phase	Catalyst source	Metal loading[a] (wt%)	Nature of carbon support	BET surface area (m^2/g)	Operating temperature (K)	Ref.
				Single reactant				
Chlorobenzene	Pd/C	Gas	Commercial	0.5	Carbon	750[b]	413	[10]
			Lab. synth.[c]	6.9; 11.0	Carbon	140; 209[b]	423; 473	[28]
		Liquid	Lab. synth.	0.72; 0.88	Carbon	1200[d]	303	[11]
			Lab. synth.	0.72; 2.7	Carbon	1200[d]	303	[45]
			Lab. synth.	Not given	Carbon (sibunit)	Not given	323	[14]
		Not given[e]	Commercial	5.0	Carbon	Not given	573	[47]
	Pd–Fe/C	Gas	Lab. synth.	Pd: 5.4–6.8; Fe: 3.6–11.1	Carbon	331–370[b]	423; 473	[28]
	Pd–Ni/C	Liquid	Lab. synth.	Not given	Carbon (sibunit)	Not given	323	[14]
Dichlorobenzenes	Pd/C	Gas	Lab. synth.	0.2	Carbon (sibunit)	372[d]	523	[44]
		Not given[d]	Commercial	5.0	Carbon	Not given	573	[47]
Trichlorobenzenes	Pd/C	Gas	Lab. synth.	0.2	Carbon (sibunit)	372[d]	523	[44]
		Liquid	Commercial	5.0	Carbon	Not given	313–355	[12]
Hexachlorobenzene	Pd/C	Liquid	Lab. synth.	0.4	Carbon (sibunit)	370[d]	323	[13]
	Pd–Ni/C	Liquid	Lab. synth.	Pd: 0.19–0.7; Ni: 0.19–2.98	Carbon (sibunit)	370[d]	323	[13]
Chlorophenols	Pd/C	Gas	Lab. synth.	2.5–8.0	Activated carbon (granular)	800–1140[b]; 1200[d]	328–473	[29]
		Liquid	Lab. synth.	2.5–8.0	Activated carbon (granular)	800–1140[b]; 1200[d]	300; 325	[29]
	Pd/ACC[f]	Liquid	Not given	0.5–5.0	Activated carbon cloth	Not given	333	[48]
			Lab. synth.	0.1–5.1	Activated carbon cloth	1540; 1560[d]	303–358	[30]
	Pd/GAC[g]	Liquid	Not given	0.5	Granulated activated carbon	Not given	333	[48]
			Lab. synth.	0.1–0.5	Activated carbon (granular)	800[d]	303–358	[30]
Dichlorophenols	Pd/C	Liquid	Commercial	1.0–10.0	Activated carbon	Not given	303	[49]
Chlorobiphenyls	Pd/C	Liquid	Commercial	10.0	Carbon	Not given	293	[50]
Dichloro-dibenzo-dioxin	Pd/C	Liquid	Commercial	5.0	Carbon	Not given	296–308	[51]
			Commercial	5.0	Carbon	1088[b]	303–318	[31]
Tetrachloro-dibenzo-dioxin	Pd/C	Liquid	Commercial	5.0	Carbon	Not given	296–308	[51]
			Commercial	5.0	Carbon	1088[b]	303–318	[31]
Dichloro-dibenzo-furan	Pd/C	Liquid	Commercial	5.0	Carbon	1088[b]	303–318	[31]
Trichloro-dibenzo-furan	Pd/C	Liquid	Commercial	10.0	Activated carbon	900–1000[b]	323	[52]
Chlorotoluenes	Pd/C	Not given[e]	Commercial	5.0	Carbon	Not given	573	[47]
Chlorobenzonitriles	Pd/C	Not given[e]	Commercial	5.0	Carbon	Not given	573	[47]
Chloroanilines	Pd/C	Not given[e]	Commercial	5.0	Carbon	Not given	573	[47]
Chloroanisoles	Pd/C	Not given[e]	Commercial	5.0	Carbon	Not given	573	[47]
Chloroacetophenones	Pd/C	Liquid	Commercial	10.0	Carbon	Not given	323	[53]
		Not given[e]	Commercial	5.0	Carbon	Not given	573	[47]
Chlorohydroxydiphenyl ethers	Pd/C	Liquid	Commercial	5.0	Carbon	Not given	298–343	[54]
				Mixed reactant feed				
(PCDDs + PCDFs)[h]	Pd/C	Liquid	Commercial	10.0	Activated carbon	900–1000[b]	323	[52]
Mixture[i]	Pd/C	Liquid	Commercial	5.0	Carbon	Not given	355	[12]
Dichlorobenzene + methylthiophene	Pd sulfide/C	Gas	Lab. synth.	9.2	Activated carbon	1100[d]	573	[55]

[a] Pd loading unless stated otherwise.
[b] Catalyst surface area.
[c] Lab. synth., laboratory synthesized.
[d] Support surface area.
[e] H_2 pressure, 1 MPa.
[f] ACC, fibrous activated carbon cloth.
[g] GAC, granulated activated carbon.
[h] PCDD, polychlorinated dibenzo-*p*-dioxins; PCDF, polychlorinated dibenzofurans.
[i] Mixture – chlorobenzene, bromobenzene, fluorobenzene and iodobenzene.

particles in a cylinder with a diameter six times greater than the particles. Temperature-programmed reduction (TPR), H_2 chemisorption, and temperature-programmed desorption (TPD), both before and after reaction, were determined using the commercial CHEM-BET 3000 (Quantachrome) unit; raw data were reproducible to better than ±6%. The samples (ca. 0.1 g) were loaded into a U-shaped Pyrex glass cell (10 cm × 3.76 mm i.d.) and contacted at room temperature with a 20 $cm^3\,min^{-1}$ (mass flow controlled) 5% v/v H_2/N_2 flow for 1 h before heating to 523 K at 10 $K\,min^{-1}$, with the effluent gas directed through a liquid N_2 trap. H_2 consumption was monitored by a thermal conductivity detector (TCD) with data acquisition/manipulation using the TPR Win™ software. The samples were maintained at 523 K for 1 h in a steady flow of H_2. The reduced samples were swept with a flow of N_2 for 1 h, cooled to room temperature, and subjected to H_2 chemisorption using a pulse (50 µl) titration procedure [5]. The samples were then thoroughly flushed with N_2 for 30 min to remove physisorbed H_2, and TPD was conducted in the N_2 flow at 50 $K\,min^{-1}$ to 873 K. Precursor reduction was also monitored using a Seiko Instruments TG/DTA 320 simultaneous thermo-gravimetric/differential thermal analyzer coupled to a Micromass PC residual gas analyzer. A known quantity of catalyst (ca. 25 mg) was placed in a Pt sample pan, and an equivalent quantity of SiO_2 was used as reference material. The sample was kept at room temperature in flowing He (100 $cm^3\,min^{-1}$) for 15 min, H_2 was introduced (20 $cm^3\,min^{-1}$), and the system was maintained at room temperature for another 30 min before heating at a rate of 1 $K\,min^{-1}$ to a final temperature of 523 K, while monitoring the effluent gas over the m/e range 10–100.

Powder X-ray diffraction (XRD) was performed with a Philips X'Pert instrument using Ni-filtered Cu-K_α radiation. The samples were mounted in a low-background sample holder and scanned at a rate of 0.02° $step^{-1}$ over the $20 \leqslant 2\theta \leqslant 90°$ range with a scan time of 5 $s\,step^{-1}$. The diffractograms were compared with the JCPDS-ICDD references [66] for identification purposes. The Pd particle morphology and size distributions were determined by transmission electron microscopy: a JEOL 2000 TEM microscope operated at an accelerating voltage of 200 kV. The catalyst sample was dispersed in 1-butanol by ultrasonic vibration and deposited on a lacey-carbon/Cu grid (200 mesh) and dried at 383 K for 12 h before TEM analysis. At least 500 individual Pd particles were counted for each catalyst; the mean Pd particle sizes are quoted in this paper as both a number average diameter ($\bar{d}_n$),

$$\bar{d}_n = \sum_i n_i d_i \Big/ \sum_i n_i, \tag{1}$$

and surface area-weighted diameter ($\bar{d}_s$) [67],

$$\bar{d}_s = \sum_i n_i d_i^3 \Big/ \sum_i n_i d_i^2, \tag{2}$$

where n_i is the number of particles of diameter d_i and $\sum_i n_i > 500$. Analysis by scanning electron microscopy (SEM) was done using a Hitachi S900 field emission SEM, operated at an accelerating voltage of 25 kV; the sample was deposited on a standard aluminum SEM holder and coated with gold. Carbon support structural characteristics were also probed by temperature-programmed oxidation (TPO), in which a 100-mg sample of demineralized support was heated (10 $K\,min^{-1}$) to 1248 K in a 5% v/v O_2/He mixture with on-line TCD analysis of the effluent gas. The equivalent pH of the three Pd catalysts was determined by standard acid–base titration. A known mass (40 mg) of each catalyst was immersed in a 50 cm^3 solution (deionized water, electronic resistance ⩾ 15 MΩ) of 0.1 $mol\,dm^{-3}$ NaCl and 0.1 $mmol\,dm^{-3}$ oxalic acid, acidified (pH = 3–4) with 0.01 $mol\,dm^{-3}$ HCl. A 0.01 $mol\,dm^{-3}$ NaOH solution was used as titrant, added dropwise (3–6 $cm^3\,h^{-1}$, model 100 kd Scientific microprocessor-controlled infusion pump) to the slurry, which was kept under continuous agitation in a He atmosphere. The pH was monitored continuously using a Dow–Corning pencil electrode coupled to a data logging and collection system (Pico Technology); reproducibility of the measurements was within ±4%.

2.3. Catalysis procedure

Reactions were carried out under atmospheric pressure in a fixed bed glass reactor (15 mm i.d.) with a co-current flow of CB in H_2 at 423 K. The catalytic reactor, and operating conditions to ensure negligible heat/mass transport limitations, have been described in detail elsewhere [68,69], but some features, pertinent to this study, are given here. The CB HDC performance of the three carbon-supported Pd catalysts was assessed over four reaction cycles with an inlet Cl to catalyst ratio = 0.24 $mol_{Cl}\,g^{-1}\,h^{-1}$. In the first cycle, the reaction was conducted (directly after catalyst activation) for 6 h, followed by reactivation in flowing H_2 at 523 K for 12 h with a second 6 h reaction cycle at 423 K, a further H_2 reactivation overnight at 523 K with a third reaction cycle at 423 K, followed in this case by overnight H_2 treatment at 423 K and a final fourth reaction cycle at 423 K. CB (>99.8% purity, Sigma–Aldrich) was fed using a microprocessor-controlled infusion pump (model 100, kd Scientific) through a glass/Teflon air-tight syringe and a Teflon line to the reactor in a stream of ultrapure H_2 ($GHSV = 2 \times 10^4$), the flow rate of which was monitored using a Humonics 520 digital flow meter. As a blank test, passage of CB in a stream of H_2 through the empty reactor (i.e., in the absence of catalyst) did not result in any detectable conversion. The reaction products were analyzed by capillary GC as described elsewhere [68,69]. The relative peak area % was converted to mol% using regression equations based on detailed calibration, and the detection limit typically corresponded to a feedstock conversion <0.4 mol%; overall analytic reproducibility was better than ±5%. The degree of hydrodechlorination (x_{Cl}) is given by

$$x_{Cl} = \frac{[HCl]_{out}}{[Cl_{org}]_{in}}, \tag{3}$$

where [Cl_{org}] represents the concentration (mol dm^{-3}) of chlorine associated with the aromatic feed and subscripts in and out refer to the inlet and outlet reactor streams, respectively. Repeated catalytic runs with different samples from the same batch of catalyst delivered product compositions that were reproducible to within ±7%.

3. Results and discussion

3.1. Catalyst characterization: prereaction

The BET surface areas, total pore volume, and average pore radii of the three freshly activated (unused) catalysts are recorded in Table 2. The raw adsorption/desorption isotherms, shown in Fig. 1a, are consistent with type IV (IUPAC classification) multilayer adsorption/desorption accompanied by capillary condensation to generate hysteresis loops that are diagnostic of mesoporosity; the associated pore size distributions (from a BJH analysis) are given in Fig. 1b. Pd/AC exhibited a high BET surface area, in keeping with the values quoted in the literature (and recorded in Table 1). The sharp increase in N_2 adsorption at low relative pressures ($P/P_0 < 0.05$) is indicative of micropore structure with an estimated 25% of the total pores with radii <2 nm. Pd/graphite is characterized by a low surface area and limited porosity, features that have mitigated against using graphite as a catalyst support. The surface area recorded for Pd/GNF is significantly greater than that of Pd/graphite, due to the greater availability of prismatic plane "edge" sites. Surface areas for carbon nanofibers have been found to range from 10 to 200 $m^2\ g^{-1}$ [65,70], depending on the synthesis parameters and postsynthesis treatment, with no apparent microporosity [65,71]. The bimodal pore size distribution that characterizes Pd/GNF in Fig. 1b was also reported by Reshetenko et al. [72] for filamentous carbon generated through methane decomposition over alumina-supported Ni, Ni/Cu, Co, and Fe–Co catalysts. A *t*-plot analysis of Pd/GNF revealed a low micropore volume (ca. 0.01 $cm^3\ g^{-1}$), which can be attributed to surface roughness, as noted elsewhere [73].

TPO is a technique that has been put to good use in probing the degree of order in carbon materials, where a move

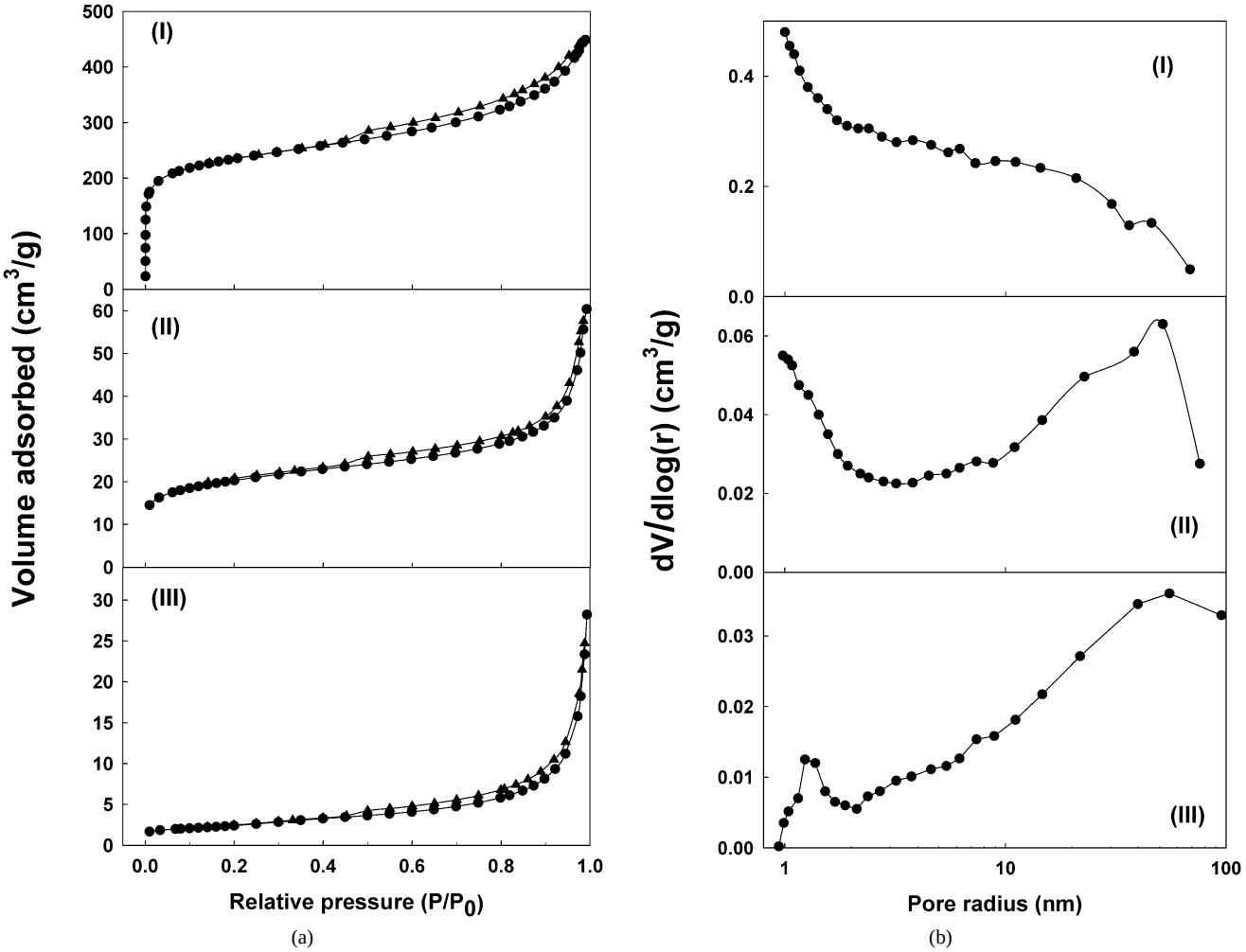

(a) (b)

Fig. 1. (a) N_2 adsorption/desorption isotherms (at 77 K) for (I) Pd/AC, (II) Pd/GNF and (III) Pd/graphite. (b) Pore size distribution, labeling as above.

Table 2
Physicochemical characteristics of the three carbon supported Pd catalysts

	Pd/AC	Pd/GNF	Pd/graphite
BET surface area ($m^2\ g^{-1}$)	875	74	11
Total pore volume ($cm^3\ g^{-1}$)	0.47	0.08	0.04
Average pore radius (nm)	3.2	4.8	9.2
Bulk density[a] ($g\ cm^{-3}$)	0.34	0.22	0.31
TPO T_{max}[a] (K)	810	1140	1220
Pd (wt%)	7.8	8.7	8.5
Equivalent pH	6.8	7.0	6.7
TPR T_{max}[b,c] (K)	377	374	375
TPR T_{max}[b,d] (K)	377	371	372
H_2 uptake ($cm^3\ g_{Pd}^{-1}$)[c]	1.0	1.7	2.2
H_2 uptake ($cm^3\ g_{Pd}^{-1}$)[d]	0.4	0.6	0.6
$\bar{d}$[c,e] (nm)	20	23	25
$\bar{d}$[d,e] (nm)	22	22	26
$\bar{d}_n$[c,f] (nm)	10	13	8
$\bar{d}_n$[d,f] (nm)	11	14	11
$\bar{d}_s$[c,g] (nm)	49	37	24
$\bar{d}_s$[d,g] (nm)	46	37	27

[a] Carbon support only.
[b] Represents negative (H_2 release) peaks.
[c] Pre-HDC.
[d] Post-HDC.
[e] Average Pd diameter based on XRD line broadening.
[f] Number average Pd diameter based on TEM analysis.
[g] Surface area-weighted Pd diameter based on TEM analysis.

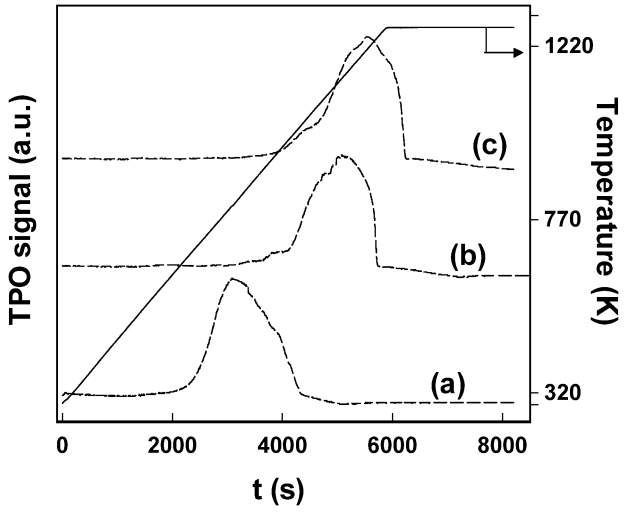

Fig. 2. TPO profiles generated for the demineralized (a) AC, (b) GNF and (c) graphite supports.

from an amorphous to a graphitic structure is accompanied by a rise in the temperature at which gasification is induced [74,75]. The TPO profiles of the GNF support, presented in Fig. 2, can be assessed against the TPO characteristics of the conventional activated carbon and graphite substrates; the characteristic T_{max} values are given in Table 2. Note that the TPO profiles were obtained from thoroughly washed and demineralized samples, to avoid any possible catalyzed gasification of carbon by residual metal. On the basis of the TPO response, the GNF substrate has significant order but is by no means as highly structured as graphite. The ordered nature of the fibers elevates the onset of gasification relative to activated carbon, but the greater presence of edge sites results in gasification at a lower temperature than graphite. Serp et al. [56] reported a comparable T_{max} (at ca. 1173 K) in their TPO analysis of fibers synthesized by C_2H_4 decomposition over Fe/SiO_2. Support structure can also be assessed by XRD analysis; diffractograms for the three supported Pd catalysts are given in Fig. 3. The XRD for Pd/graphite is dominated by a peak at 26° that is characteristic of highly structured (graphitic) carbon [66], a response that is (as expected) not present in the profile for Pd/AC. Whereas the XRD for Pd/GNF demonstrates the strong presence of a graphitic phase, the broadness of the 26° peak is indicative of a lesser long-range structural order. The extracted average d_{002} intershell spacing of 0.3349 nm differs from the value (0.3395 nm) that characterizes the graphite substrate. The deviation in d_{002} spacing is suggestive of some morphological diversity/amorphous carbon component associated with Pd/GNF. Indeed, the fibers exhibit a broad range of diameters, as illustrated in the size histogram (based on a comprehensive TEM analysis) presented in Fig. 4; mean fiber diameter is 225 nm. Because GNF diameter is largely governed by the dimensions of the seed metal particle, it is to be expected that a wide size range results from growth

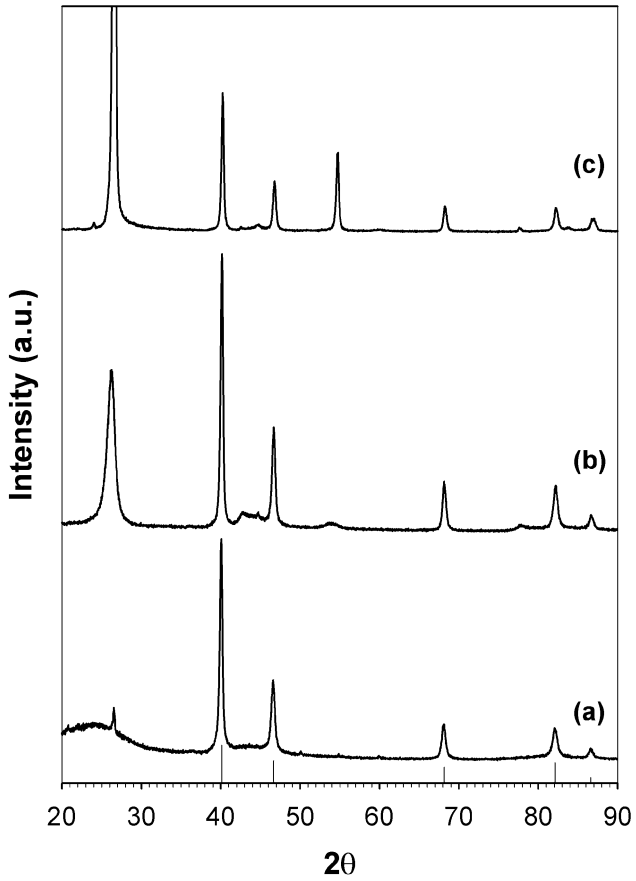

Fig. 3. XRD patterns for the activated (a) Pd/AC, (b) Pd/GNF and (c) Pd/graphite. Solid lines indicate peak position (with relative intensity) for cubic Pd.

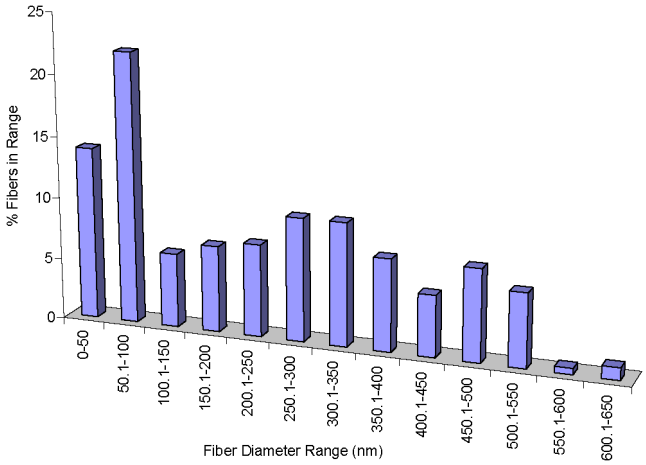

Fig. 4. Fiber diameter distribution associated with GNF.

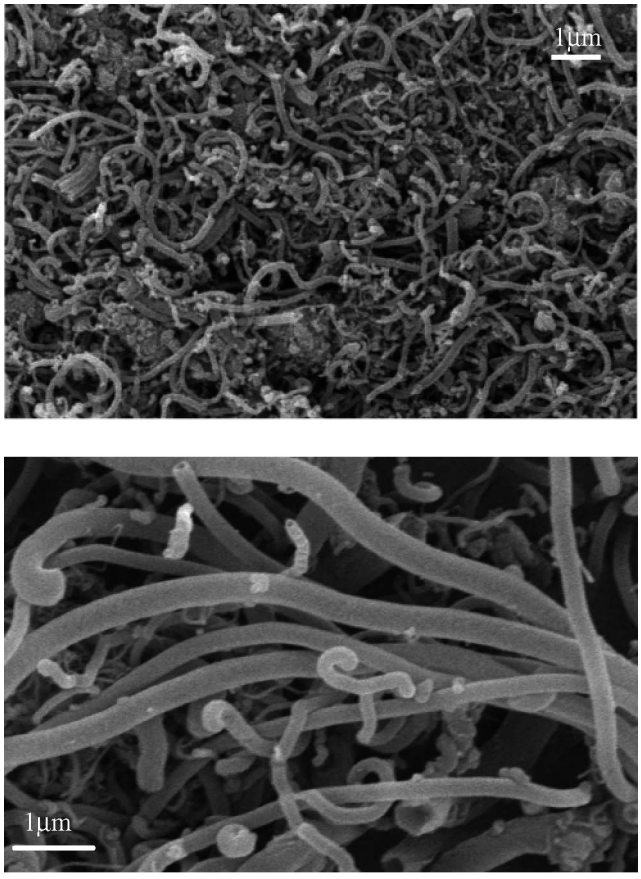

Fig. 5. Representative SEM images showing structural features associated with the GNF support.

over unsupported Ni (used in this study); using supported Ni can facilitate the production of an appreciably narrower fibrous product [76]. The high-aspect ratio fibrous nature of the GNF support is immediately apparent from the representative SEMs given in Fig. 5, which reveals a range of fiber diameters.

The TPR profiles generated for the three catalysts can be compared in Fig. 6, and the T_{max} values that characterize the

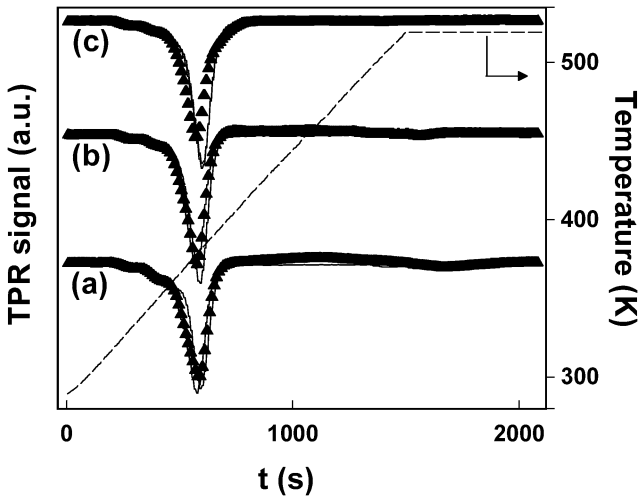

Fig. 6. TPR profiles generated for reduction of (a) Pd/AC, (b) Pd/GNF and (c) Pd/graphite pre- (solid lines) and post- (symbols) HDC.

predominant peak in each profile are recorded in Table 2; the TPR conditions match those used for actual catalyst activation before HDC. Duplicate TPR measurements are included in Fig. 6 to illustrate the level of reproducibility. Each TPR profile is dominated by a negative peak at 375 ± 2 K. There is a general consensus in the literature that Pd can absorb H_2 to form a Pd hydride at ambient temperature where H_2 partial pressure exceeds 0.0224 atm [77]. The decomposition of the Pd hydride phase has been linked to a negative peak (H_2 release) in the TPR profile where $T < 393$ K [19,23,78–82]. The absence of any obvious H_2 consumption (during TPR) in advance of H_2 release presupposes the existence of the metallic phase before the commencement of the temperature ramp. Indeed, using TGA/DTA with on-line mass spectrometry, we analyzed the effluent gas during the room temperature H_2 contact and detected small weight changes (<1%) accompanied by an exotherm that coincided with the evolution of H_2O, N_2, O_2, and (trace) N_2O, as shown in Fig. 7 for Pd/GNF; the Pd/AC and Pd/graphite systems also exhibited similar behavior. These results are diagnostic of precursor decomposition/reduction during the room temperature H_2 contact that preceded TPR, and, indeed, room temperature reduction of PdO has been proposed in the literature [82–84].

The TEM images provided in Fig. 8 serve to illustrate the nature of the Pd particle morphology and dispersion on the three carbonaceous supports; selected area electron diffraction confirmed the presence of metallic Pd. The Pd particles supported on AC exhibit an indistinct or globular geometry (Fig. 8a) that has been shown to be diagnostic of limited metal–support interaction [85]. In marked contrast, the metal phase on graphite and, to a lesser extent, on GNF can be characterized as faceted and relatively thin Pd particles, morphological features that are consistent with stronger metal–support interactions [86] (see Figs. 8b and c) and that find support in observations made by Ledoux et al. [60]. An "even" dispersion of Pd particles is evident on the GNF sub-

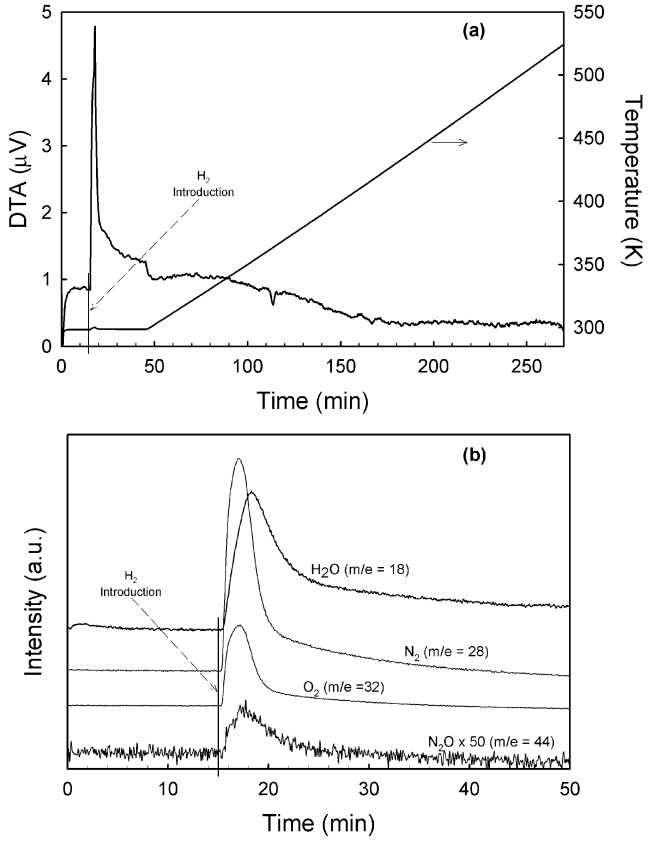

Fig. 7. (a) DTA for H_2 treatment of Pd/GNF, as a function of time and (b) residual gas analysis of the effluent gas showing an expanded time axis, representing the room temperature section of Fig. 7a. In both cases the vertical line signifies the time at which H_2 was introduced to the system.

strate. Under higher magnification, the GNF graphene layers are oriented parallel to the fiber axis; high-resolution TEM images of the GNF substrate are published elsewhere [57]. XRD analysis revealed that the Pd phase on all three supports exhibits a cubic geometry with the four peaks (see Fig. 3) at 40.1, 46.7, 68.1, and 82.15°, corresponding respectively to Pd planes (111), (200), (220), and (311). The markers identified in Fig. 3 illustrate the position and relative intensity of the XRD peaks for cubic Pd obtained from JCPDS standards [66]. Integral breadth analysis yielded similar average Pd particle diameters for each catalyst; see the entries in Table 2. The Pd particle size distributions, based on TEM analysis, are presented in the histograms in Fig. 9. The size distribution and shapes of the supported Pd particles are inherent features of the interfacial energies associated with each system. Each catalyst exhibits a broad size range, and although the average diameter values are similar, the surface-weighted values are decidedly different (see Table 2). The volume of H_2 adsorbed on the freshly activated catalysts is also given in Table 2. Although we have avoided the assignment of particle sizes based on the chemisorption measurements, because this presumes an exclusive H:Pd stoichiometry that is at best a convenient approximation, the order of increasing H_2 uptake Pd/AC < Pd/GNF < Pd/graphite follows the decreasing surface-weighted particle size sequence resulting from TEM analysis. It is intriguing that the graphite substrate with a low BET surface area and few edge positions available for depositing the metal generates the smallest surface area-weighted average Pd diameter. Xue et al. [87] reported a preparation of Pd supported on carbon "nanotubes" (diameter ca. 20 nm), graphite, and activated carbon by thermal decomposition (in H_2 up to 873 K) of $HPdCl_3$ (introduced by impregnation). On the basis of their XRD analysis, the authors claimed that the Pd phase on graphite and activated carbon shows bulk metal characteristics, whereas the nanotube stabilized nanoscale (<20 nm) Pd particles, findings that run counter to our results.

Hydrogen TPD can shed some light on differences in metal–support interaction and electronic properties of supported metal particles [69,88]; the H_2 TPD profiles are presented in Fig. 10. Each desorption profile is featureless at temperatures < 420 K with the appearance of a positive peak with an ill-defined T_{max} at 464–503 K. The volume of H_2 released (corresponding to this peak) matches that taken up in the chemisorption step that preceded TPD (see Table 2). We also recorded a second higher temperature peak (840–850 K) for the three catalysts. A direct comparison of the H_2 TPD profiles generated in this study with the limited reports in the literature on supported Pd systems is problematic given the differences in the metal loading/support/catalyst preparation/activation/desorption procedure. Ouchaib et al. [89] reported two H_2 desorption peaks from charcoal-supported Pd at 373 and 673 K. Hydrogen desorption at the higher temperatures has been attributed to spillover H_2 release [69,90,91], which can result from a combined chemisorption on the Pd and transport to the carbon support during TPR [91]. Such an assignment is consistent with the sequence of increasing peak area (i.e., Pd/graphite < Pd/GNF < Pd/AC), which mirrors the increasing BET surface area of the support (see Table 2).

3.2. Catalytic activity: HDC of CB

The HDC of CB over all three catalysts generated benzene as the predominant product, with trace amounts of cyclohexane (selectivity <3%) resulting from the further hydrogenation of benzene. Fig. 11 shows the variation of the fractional dechlorination (x_{Cl}), under identical reaction conditions, with time-on-stream (TOS). In the first reaction cycle, the initial fractional dechlorination extracted from the empirical fit (see Fig. 11) to the x_{Cl} temporal response decreased in the order Pd/GNF (0.74) ≈ Pd/AC (0.70) > Pd/graphite (0.51). A loss of activity, particularly prevalent in the case of Pd/AC, is evident with TOS, an effect that has been observed for reaction in both liquid [21,33–36] and gas phases [21,38,41] and is attributed to carbon deposition/occlusion of the active metal sites and/or surface poisoning by HCl and/or metal sintering. A resumption of the reaction after an overnight isothermal treatment (523 K, the original temperature of activation) in flowing H_2 delivered

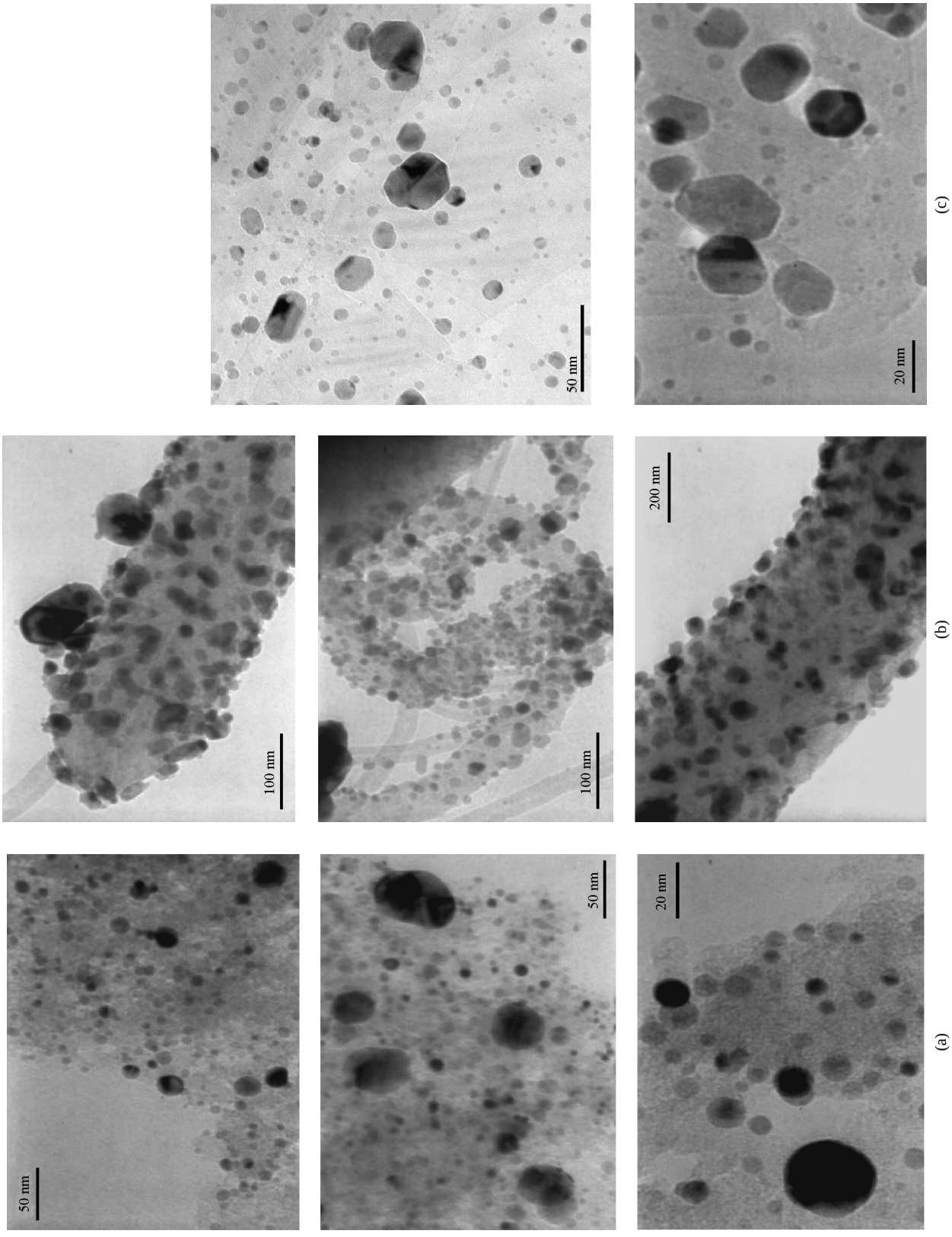

Fig. 8. Representative TEM images illustrating the nature of the supported Pd phase in (a) Pd/AC, (b) Pd/GNF and (c) Pd/graphite.

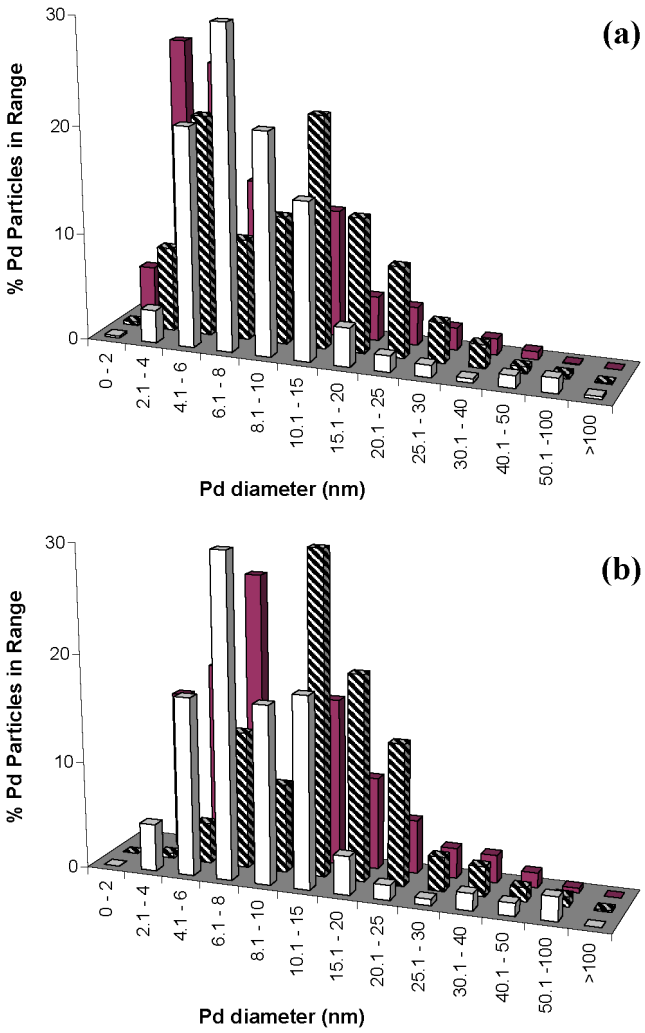

Fig. 9. Pd particle size distributions associated with Pd/AC (open bars), Pd/GNF (hatched bars) and Pd/graphite (solid bars) pre- (a) and post- (b) HDC.

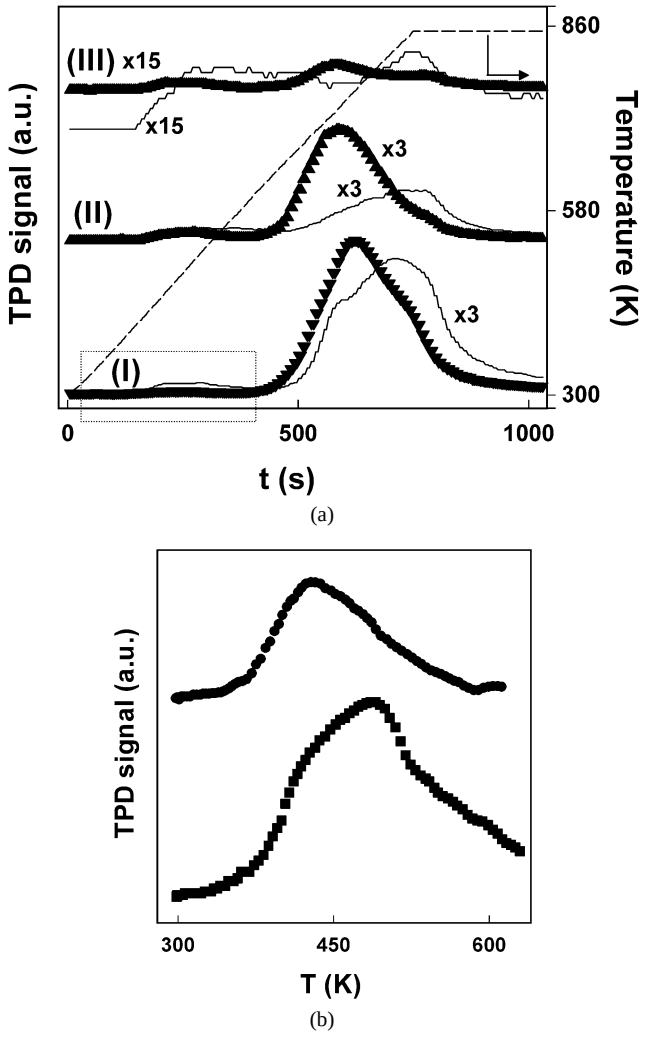

Fig. 10. (a) H_2 TPD profiles associated with (I) Pd/AC, (II) Pd/GNF and (III) Pd/graphite pre- (solid lines) and post- (symbols) HDC. (b) Expanded lower temperature region (indicated by the dotted box above) of the H_2 TPD profile for Pd/AC pre- (■) and post- (●) HDC.

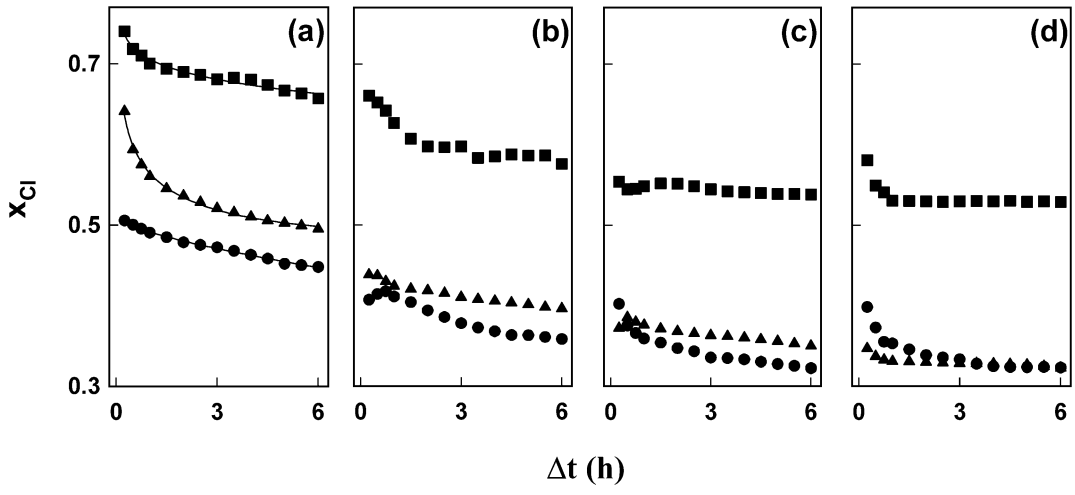

Fig. 11. Fractional CB HDC (x_{Cl}) as a function of time-on-stream over Pd/AC (▲), Pd/GNF (■) and Pd/graphite (●): (a) reaction over freshly activated catalysts; (b) following reaction (a), catalyst regeneration in H_2 at 523 K for 12 h; (c) following reaction (b), catalyst regeneration in H_2 at 523 K for 12 h; (d) following reaction (c), catalyst regeneration in H_2 at 423 K for 12 h. Lines represent fits to $x_{Cl} = (x_0\,\Delta t^n)\exp(-k\,\Delta t)$, correlation coefficients >0.996.

TOS profiles (Fig. 11b) that demonstrate a continual loss of activity. Deactivation was irreversible in that the higher-temperature H_2 treatment did not restore the original level of HDC activity. This agrees with a previous study [38] that found that a thermal H_2 treatment is insufficient to remove any strongly bound surface halogen component, although a controlled oxidation with subsequent reduction can partially restore the original HDC activity. A second attempted regeneration in H_2 at 523 K (Fig. 11c) with subsequent reaction and a final H_2 regeneration at 423 K resulted in the apparent attainment of a steady-state conversion (Fig. 11d). The ultimate x_{Cl} delivered by Pd/GNF was higher than that associated with either Pd/AC or Pd/graphite, in which HDC performance converged to a common x_{Cl}; the specific activities ($mol_{Cl}\,h^{-1}\,m^{-2}$) after 24 h on-stream follow the sequence Pd/GNF (10.9×10^{-2}) > Pd/AC (8.8×10^{-2}) > Pd/graphite (4.9×10^{-2}).

Differences in catalytic behavior associated with carbon-supported metal systems have been reported in the literature [56–58,62–64,92], notably in hydrogenation and ammonia synthesis applications, and have been attributed to metal–support interaction that impact on metal site activity; the nature of these interactions remains unclear. Pham-Huu et al. [71,92], in a comprehensive study, found that Pd supported on carbon fibers with a "fishbone" lattice orientation was more active than Pd/activated charcoal in the liquid phase hydrogenation of cinnamaldehyde. In the hydrogenation of 1-butene and 1,3-butadiene, Ni/GNF had higher activity than Ni/AC and Ni/Al_2O_3 [62], but the difference in the hydrogenation of ethylene was not as marked [63]; nevertheless, Ni/GNF consistently exhibited the best performance. Such results, although limited, indicate that the catalytic response to a shift from an amorphous to an ordered carbonaceous support is dependent on the nature of the reactants. Although an unambiguous link between catalyst structure and HDC activity has yet to emerge, several published studies have demonstrated a HDC activity and stability dependence on metal dispersion [33,93,94]. Given the commonality of Pd loading in our three catalysts, linking initial HDC performance over the first reaction cycle to surface-weighted average Pd size (Table 2) suggests a higher initial specific HDC activity for "larger" supported Pd particles. This observation is in line with the work of Juszczyk et al. [95], who reported a higher turnover frequency of both CF_3CFCl_2 and CCl_2F_2 for larger Pd particles supported on Al_2O_3, an effect that they attributed to an ensemble effect. The higher initial HDC activity associated with Pd/AC and Pd/GNF compared with Pd/graphite can also be associated (albeit tentatively) with the presumed (on the basis of TPD; see Fig. 10) higher H_2 spillover associated with the former catalysts. In support of this, there is evidence in the literature of the contribution of spillover H_2 to HDC [3,69,96]. In terms of CB activation, it is known that haloarenes can adsorb both on the metal phase [21,38] and on the carbon support [97–100]. In terms of the former, we recorded a 45% conversion (of 33 $mol_{CB}\,h^{-1}\,cm^{-3}$ Pd at 423 K) over bulk Pd; that is, the metal phase alone can serve to activate CB with H_2 dissociation and subsequent HDC. In liquid phase chloroarene adsorption applications [101], GNF (with no associated metal phase) outperformed conventional activated and graphitic carbon, an effect ascribed to high conductivity and greater availability of delocalized π-electrons associated with GNF. Acid-washing of the carbon substrate was also found to affect uptake as a result of the increased surface concentration of oxygenated functional groups/electron rich regions that can participate in the formation of electron donor–acceptor complexes with the aromatic sorbate. Toebes et al. [102] found that the liquid phase cinnamaldehyde hydrogenation activity associated with GNF-supported Ru increased significantly after removal of surface acid groups; the number of surface acid sites was in the range 0.02–0.62 nm^{-2}. The acid washing done in this study to remove the seed Ni particles was far less severe where acid/base titration delivered near-neutral surface-equivalent pH values for the three catalysts (see Table 2). Differences in surface "acidity" do not explain the activity sequence. Consider the work of Santoro and Louw [103], who showed that AC alone was capable of promoting gas phase HDC of CB at temperatures >573 K. But we did not detect any CB HDC activity over the three carbon supports (in the absence of a metal phase) under our stated reaction conditions. Our observed HDC activities can be considered the result of contributions from the supported Pd, the carbon substrate, and the Pd–carbon interface. We cannot explicitly identify a unique catalyst characteristic that determines HDC activity, but there are strong indications that Pd particle size and H_2 spillover contribute to HDC performance. In our study this response is somewhat masked by the appreciable loss of activity suffered by Pd/AC. Metal–support interaction(s) can affect temporal HDC behavior, where, based on our results, a faceting of Pd particles (on GNF and graphite) appears to favor HDC stability.

3.3. Catalyst characterization: postreaction

Because the three Pd catalysts exhibited a TOS HDC activity loss, the used catalysts were also subjected to characterization to account for this decline in performance. There was no detectable change in the BET surface area/porosity of each catalyst after the four cycles of CB HDC. Moreover, chemical analysis (ICP-OES) of the activated catalysts before and after reaction did not reveal any measurable loss of Pd as a result of the catalysis sequence. The TPR characteristics of the spent samples (shown in Fig. 6) did not deviate significantly from the profiles associated with the unused samples and are dominated by the negative peak associated with Pd hydride decomposition. Hydrogen uptake on the used catalysts was lower (see Table 2) by up to a factor of three, an effect suggesting decreased metal dispersion; metal agglomeration during HDC has been noted elsewhere [3,40,88]. However, in this study both the Pd number-averaged and surface area-averaged diameters (Table 2) showed little difference after reaction. Nevertheless, it is worth compar-

ing the Pd size distributions for the unused (Fig. 9a) and used (Fig. 9b) catalysts; doing so clearly shows that the percentage of particles <6 nm is lower in the used samples, with a corresponding increase in the proportion within the range 10–20 nm, diagnostic of some, albeit limited (particularly in the case of Pd/AC), particle growth. XRD analysis of the spent samples did not reveal any structural (or significant particle size) changes; based on our comprehensive TEM analysis, we can state that the Pd particle morphology remained unchanged after reaction. A preponderance of faceted particles remained associated with Pd/graphite, a virtually exclusive globular morphology characterized Pd/AC, whereas Pd/GNF exhibited both faceted and nonfaceted particles. Suppression of H_2 uptake may result from prolonged contact with CB, in that Cl is known to limit the degree of H_2 chemisorption on supported transition metals [22]. Bonarowska et al. [80] reported substantial carbon dissolution in the supported Pd phase during CFC HDC. Although we did not observe (on the basis of XRD analysis) bulk Pd carbide formation, the presence of occluding carbonaceous species as result of HDC may well affect H_2 uptake. This may also influence the H_2 TPD response, which can be assessed by evaluating Fig. 10, in which the low-temperature desorption peak is shifted in each case to a lower temperature, indicative of a weaker surface interaction. This is illustrated in Fig. 10b for Pd/AC, where the H_2 TPD T_{max} is lowered from ca. 490 to 430 K after the four HDC cycles. The higher temperature desorption peak was also shifted (by up to 100 K) to lower temperatures after HDC, again indicative of some surface modification. Surprisingly, the amount of H_2 released, corresponding to this TPD peak, was significantly greater than that recorded before HDC. This was particularly evident in the case of Pd/AC and less so for the lower BET surface area Pd/GNF and Pd/graphite. We have shown elsewhere [3,88] that supported metal catalysts bear an appreciable surface HCl component during chloroarene HDC, some of which is irreversibly held and resistant to thermal desorption. It has been demonstrated [103] that a dissociative adsorption of chloroarenes on carbon results in both aryl moiety and chemical bonding of Cl to the surface, where temperatures in excess of 773 K are needed to induce desorption. Hydrogen spillover behavior in supported metals systems can be disrupted by the presence of surface Cl [104], which enhances spillover, possibly due to formation of a mobile proton–electron pair [105]. Given the equivalency of the total catalyst surface areas before and after HDC, we tentatively attribute the increase in H_2 TPD to residual surface Cl species that promote spillover of weakly bound hydrogen onto the support. This disruption of surface hydrogen is accompanied by a loss of HDC activity.

4. Conclusions

In the HDC of CB over carbon-supported Pd (8 ± 1 wt%), the nature of the carbon (unstructured AC vs. structured graphite and GNF) has a considerable impact on catalytic activity. The GNF-supported Pd exhibited the highest HDC activity, which also proved to be the most stable. The commercial AC support has a high-surface area (875 $m^2\,g^{-1}$) with a significant micropore component. The commercial graphite is characterized by low surface area (11 $m^2\,g^{-1}$) and limited porosity, whereas GNF (synthesized by ethylene decomposition over unsupported Ni) has an intermediate surface area (74 $m^2\,g^{-1}$) and negligible microporosity; all three catalysts exhibit a near-neutral surface-equivalent pH. The high-aspect ratio GNF substrate (on the basis of TEM and TPO analysis) is crystalline in nature, with a structural order approaching that of graphite. HDC of CB yields benzene as the predominant product (with secondary hydrogenation to cyclohexane), where initial HDC activity increased in the order Pd/graphite < Pd/AC ≈ Pd/GNF. The supported Pd exhibited a cubic geometry in which the surface area-weighted average diameter decreases in the order Pd/AC > Pd/GNF > Pd/graphite, which matches the sequence of increasing H_2 uptake. Pd particles on AC displayed a globular morphology, whereas the supported Pd phase on graphite (in particular) and GNF (to a lesser extent) was faceted, diagnostic of stronger metal–support interactions. Each catalyst was subject to an irreversible loss of activity that was more extreme in the case of Pd supported on amorphous carbon. The structured carbon substrates served to stabilize Pd HDC activity to a greater extent; after four HDC reaction/thermal regeneration cycles, Pd/GNF delivered the highest (by a factor of up to 2.4) steady-state specific HDC activity. Our catalytic data when coupled to pre-HDC and post-HDC characterization results suggest that HDC activity is enhanced over larger Pd particles and that loss of activity is accompanied by disrupted hydrogen adsorption/desorption surface dynamics.

Acknowledgments

The authors thank Lourdes Astillero and Dr. Colin Park for their contribution to this work, which was supported in part by the National Science Foundation (Grant CTS-0218591).

References

[1] E. Goldberg, Sci. Total Environ. 100 (1991) 17.
[2] Environmental Protection Agency, OPPT Chemical Fact Sheets. Pollution Prevention and Toxics (7407). EPA 749-F-95-007a. Support Document: CAS No. 108-90-7 (1995).
[3] M.A. Keane, in: M.A. Keane (Ed.), Interfacial Applications in Environmental Engineering, Marcel Dekker, New York, 2002, p. 231.
[4] C. Menini, C. Park, E.-J. Shin, G. Tavoularis, M.A. Keane, Catal. Today. 62 (2000) 355.
[5] K.V. Murthy, P.M. Patterson, G. Jacobs, B.H. Davis, M.A. Keane, J. Catal. 223 (2004) 74.
[6] L.N. Zanaveskin, V.A. Aver'yanov, Russ. Chem. Rev. 67 (1998) 713.
[7] L.N. Zanaveskin, V.A. Aver'yanov, Y.A. Treger, Russ. Chem. Rev. 65 (1996) 617.

[8] R. Louw, J.W. Rothuizen, R.C.C. Wegman, J. Chem. Soc., Perkin Trans. 2 (1973) 1635.
[9] J.A. Manion, P. Mulder, R. Louw, Environ. Sci. Technol. 19 (1985) 280.
[10] L. Prati, M. Rossi, Appl. Catal. B: Environ. 23 (1999) 135.
[11] J.L. Benitez, G. Angel, React. Kinet. Catal. Lett. 70 (2000) 67.
[12] Y. Ukisu, T. Miyadera, J. Mol. Catal. A: Chem. 125 (1997) 135.
[13] V. Simagina, V. Likholobov, G. Bergeret, M.T. Gimenez, A. Renouprez, Appl. Catal. B: Environ. 40 (2003) 293.
[14] V.A. Yakovlev, V.V. Terskikh, V.I. Simagina, V.A. Likholobov, J. Mol. Catal. A: Chem. 153 (2000) 231.
[15] Y. Cesteros, P. Salagre, F. Medina, J.E. Sueiras, Appl. Catal. B: Environ. 22 (1999) 135.
[16] M.A. Keane, G. Tavoularis, React. Kinet. Catal. Lett. 78 (2003) 11.
[17] P.P. Kulkarni, S.S. Deshmukh, V.I. Kovalchuk, J.L. d'Itri, Catal. Lett. 61 (1999) 161.
[18] B.F. Hagh, D.T. Allen, Chem. Eng. Sci. 45 (1990) 2695.
[19] N. Lingaiah, P.S.S. Prasad, P.K. Rao, F.J. Berry, L.E. Smart, Catal. Commun. 3 (2002) 391.
[20] I.V. Mishakov, V.V. Chesnokov, R.A. Buyanov, N.A. Pakhomov, Kinet. Catal. 42 (2001) 543.
[21] F.J. Urbano, J.M. Marinas, J. Mol. Catal. A: Chem. 173 (2001) 329.
[22] D.J. Moon, M.J. Chung, K.Y. Park, S.I. Hong, Appl. Catal. A: Gen. 168 (1998) 159.
[23] S.C. Shekar, J.K. Murthy, P.K. Rao, K.S.R. Rao, Catal. Commun. 4 (2003) 39.
[24] S. Ordonez, H. Sastre, F.V. Diez, Appl. Catal. B: Environ. 25 (2000) 49.
[25] S. Ordonez, F.V. Diez, H. Sastre, Ind. Eng. Chem. Res. 41 (2002) 505.
[26] G. Tavoularis, M.A. Keane, J. Mol. Catal. A: Chem. 142 (1999) 187.
[27] G. Tavoularis, M.A. Keane, Appl. Catal. A: Gen. 182 (1999) 309.
[28] N. Lingaiah, M. Uddin, A. Muto, Y. Sakata, J. Chem. Soc. Chem. Commun. (1999) 1657.
[29] Y. Matatov-Meytal, M. Sheintuch, Ind. Eng. Chem. Res. 39 (2000) 18.
[30] Y. Shindler, Y. Matatov-Meytal, M. Sheintuch, Ind. Eng. Chem. Res. 40 (2001) 3301.
[31] Y. Ukisu, T. Miyadera, Appl. Catal. B: Environ. 40 (2003) 141.
[32] C. Schuth, M. Reinhard, Appl. Catal. B: Environ. 18 (1998) 215.
[33] M.A. Aramendia, V. Borau, I.M. Garcia, C. Jimenez, F. Lafont, A. Marinas, J.M. Marinas, F.J. Urbano, J. Catal. 187 (1999) 392.
[34] R. Gopinath, K.N. Rao, P.S.S. Prasad, S.S. Madhavendra, S. Narayanan, G. Vivekanandan, J. Mol. Catal. A: Chem. 181 (2002) 215.
[35] M.A. Aramendia, V. Borau, I.M. Garcia, C. Jimenez, F. Lafont, A. Marinas, J.M. Marinas, F.J. Urbano, J. Mol. Catal. A: Chem. 184 (2002) 237.
[36] M.A. Aramendia, R. Burch, I.M. Garcia, A. Marinas, J.M. Marinas, B.W.L. Southward, F.J. Urbano, Appl. Catal. B: Environ. 31 (2001) 163.
[37] E. Lopez, S. Ordonez, H. Sastre, F.V. Diez, J. Hazard. Mater. 97 (2003) 281.
[38] B. Coq, G. Ferrat, F. Figueras, J. Catal. 101 (1986) 434.
[39] P. Bodnariuk, B. Coq, G. Ferrat, F. Figueras, J. Catal. 116 (1989) 459.
[40] A. Gampine, D.P. Eyman, J. Catal. 179 (1998) 315.
[41] S. Jujjuri, E. Ding, S.G. Shore, M.A. Keane, Appl. Organomet. Chem. 17 (2003) 493.
[42] F.J. Berry, L.E. Smart, P.S.S. Prasad, N. Lingaiah, P.K. Rao, Appl. Catal. A: Gen. 204 (2000) 191.
[43] N. Lingaiah, P.S.S. Prasad, P.K. Rao, L.E. Smart, F.J. Berry, Appl. Catal. A: Gen. 213 (2001) 189.
[44] S.B. Halligudi, B.M. Devassay, A. Ghosh, V. Ravikumar, J. Mol. Catal. A: Chem. 184 (2002) 175.
[45] G. del Angel, J.L. Benitez, J. Mol. Catal. A: Chem. 165 (2001) 9.
[46] L. Lassova, H.K. Lee, T.S.A. Hor, J. Mol. Catal. A: Chem. 144 (1999) 397.
[47] K. Konuma, N. Kameda, J. Mol. Catal. A: Chem. 178 (2002) 239.
[48] Y. Matatov-Meytal, M. Sheintuch, Catal. Today 75 (2002) 63.
[49] G. Yuan, M.A. Keane, Chem. Eng. Sci. 58 (2003) 257.
[50] H. Sajiki, A. Kume, K. Hattori, K. Hirota, Tetrahedron Lett. 43 (2002) 7247.
[51] Y. Ukisu, T. Miyadera, Chemosphere 46 (2002) 507.
[52] P. Tundo, A. Perosa, M. Selva, S.S. Zinovyev, Appl. Catal. B: Environ. 32 (2001) L1.
[53] P. Tundo, S. Zinovyev, A. Perosa, J. Catal. 196 (2000) 330.
[54] C. Xia, J. Xu, W. Wu, Q. Luo, J. Chen, Q. Zhang, X. Liang, Appl. Catal. B: Environ. 45 (2003) 281.
[55] J. Frimmel, M. Zdrazil, J. Catal. 167 (1997) 286.
[56] P. Serp, M. Corrias, P. Kalck, Appl. Catal. A: Gen. 253 (2003) 337.
[57] C. Park, M.A. Keane, J. Colloid Interface Sci. 266 (2003) 183.
[58] J.M. Planeix, N. Coustel, B. Coq, V. Brotons, P.S. Kumbhar, R. Dutartre, P. Geneste, P. Bernier, P.M. Ajayan, J. Am. Chem. Soc. 116 (1994) 7935.
[59] J.-M. Nhut, L. Pesant, J.-P. Tessonnier, G. Winé, J. Guille, C. Pham-Huu, M.-J. Ledoux, Appl. Catal. A: Gen. 254 (2003) 345.
[60] M.J. Ledoux, R. Vieira, C. Pham-Huu, N. Keller, J. Catal. 216 (2003) 333.
[61] D.S. Cameron, S.J. Cooper, I.L. Dodgson, B. Harrison, J.W. Jenkins, Catal. Today 7 (1990) 113.
[62] A. Chambers, T. Nemes, N.M. Rodriguez, R.T.K. Baker, J. Phys. Chem. B 102 (1998) 2251.
[63] C. Park, R.T.K. Baker, J. Phys. Chem. B 102 (1998) 5168.
[64] C. Liang, Z. Li, J. Qiu, C. Li, J. Catal. 211 (2002) 278.
[65] K.P. de Jong, J.W. Geus, Catal. Rev.-Sci. Eng. 42 (2000) 481.
[66] JCPDS–ICDD, PCPDFWIN, Version 2.2, June 2001.
[67] N. Krishnankutty, M.A. Vannice, J. Catal. 155 (1995) 312.
[68] G. Tavoularis, M.A. Keane, J. Chem. Technol. Biotechnol. 74 (1999) 60.
[69] E.-J. Shin, A. Spiller, G. Tavoularis, M.A. Keane, Phys. Chem. Chem. Phys. 1 (1999) 3173.
[70] M.L. Toebes, J.A. van Dillen, K.P. de Jong, J. Mol. Catal. A: Chem. 173 (2001) 75.
[71] C. Pham-Huu, N. Keller, G. Ehret, L.J. Charbonniere, R. Ziessel, M.J. Ledoux, J. Mol. Catal. A: Chem. 170 (2001) 155.
[72] T.V. Reshetenko, L.B. Avdeeva, Z.R. Ismagilov, V.V. Pushkarev, S.V. Cherpanova, A.L. Chuvilin, V.A. Likholobov, Carbon 41 (2003) 1605.
[73] M.L. Toebes, J.H. Bitter, A.J. van Dillen, K.P. de Jong, Catal. Today 76 (2002) 33.
[74] D.W. McKee, in: P.L. Walker Jr., P.A. Thrower (Eds.), Chemistry and Physics of Carbon, vol. 16, Marcel Dekker, New York, 1981, p. 1.
[75] C. Park, M.A. Keane, Chem. Phys. Chem. 2 (2001) 733.
[76] C. Park, P.M. Patterson, M.A. Keane, Curr. Top. Colloid. Interface Sci. 5 (2002) 92.
[77] J.E. Benson, H.S. Hwang, M. Boudart, J. Catal. 30 (1973) 146.
[78] N.K. Nag, J. Phys. Chem. 105 (2001) 5945.
[79] G. Neri, M.G. Musolino, C. Milone, D. Pietropaolo, S. Galvagno, Appl. Catal. A: Gen. 208 (2001) 307.
[80] M. Bonarowska, J. Pielaszek, V.A. Semikolenov, Z. Karpinski, J. Catal. 209 (2002) 528.
[81] L.M. Gomez-Sainero, X.L. Seoane, J.L.G. Fierro, A. Arcoya, J. Catal. 209 (2002) 279.
[82] C.B. Wang, H.K. Lin, C.M. Ho, J. Mol. Catal. A: Chem. 180 (2002) 285.
[83] G.M. Tonetto, D.E. Damiani, J. Mol. Catal. A: Chem. 202 (2003) 289.
[84] F. Pinna, F. Menegazzo, M. Signoretto, P. Canton, G. Fagherazzi, N. Pernicone, Appl. Catal. A: Gen. 219 (2001) 195.
[85] R.T.K. Baker, E.B. Prestridge, R.L. Garten, J. Catal. 59 (1979) 293.
[86] C. Park, R.T.K. Baker, J. Phys. Chem. B 103 (1999) 2453.
[87] B. Xue, P. Chen, Q. Hong, J. Lin, K.L. Tan, J. Mater. Chem. 11 (2001) 2378.
[88] C. Park, C. Menini, J.L. Valverde, M.A. Keane, J. Catal. 211 (2002) 451.

[89] T. Ouchaib, B. Moraweck, J. Massardier, A. Renouprez, Catal. Today 7 (1990) 191.
[90] Z.X. Cheng, S.B. Yuan, J.W. Fan, Q.M. Zhu, M.S. Zhen, Stud. Surf. Sci. Catal. 112 (1997) 261.
[91] W.C. Conner Jr., J.L. Falconer, Chem. Rev. 95 (1995) 759.
[92] C. Pham-Huu, N. Keller, L. J Charbonniere, R. Ziessel, M.J. Ledoux, Chem. Commun. (2000) 1871.
[93] Z.C. Zhang, B.C. Beard, Appl. Catal. A: Gen. 174 (1998) 33.
[94] M.A. Keane, C. Park, C. Menini, Catal. Lett. 88 (2003) 89.
[95] W. Juszczyk, A. Mallinowski, Z. Karpinski, Appl. Catal. A: Gen. 166 (1998) 311.
[96] S. Kovenklioglu, Z. Cao, D. Shah, R.J. Farrauto, E.N. Balko, AIChE J. 38 (1992) 1003.
[97] L.C.A. Oliveira, R.V.R.A. Rios, J.D. Fabris, V. Garg, K. Sapag, R.M. Lago, Carbon 40 (2002) 2177.
[98] V.I. Zheivot, E.M. Moroz, V.I. Zaikovskii, V.V. Chesnokov, V.Yu. Gavrilov, J. Chromatogr. A. 786 (1997) 117.
[99] H. Lorbeer, S. Starke, M. Gozan, A. Tiehm, P. Werner, Water, Air, Soil Pollut. 2 (2002) 183.
[100] I.E. Fangmark, L.G. Hammarstrom, M.E. Stromqvist, A.L. Ness, P.R. Norman, N.M. Osmond, Carbon 40 (2002) 2861.
[101] M.A. Keane, Green Chem. 5 (2003) 309.
[102] M.L. Toebes, F.F. Prinsloo, J.H. Bitter, A.J. van Dillen, K.P. de Jong, J. Catal. 214 (2003) 78.
[103] D. Santoro, R. Louw, Carbon 39 (2001) 2091.
[104] P.A. Sermon, G.C. Bond, Catal. Rev. 8 (1973) 211.
[105] B.K. Hodnett, B. Delmon, Stud. Surf. Sci. Catal. 27 (1986) 53.